Supporting Information

Realizing the Synergy of Sn Cluster Incorporation and Nitrogen Doping for Carbonaceous Hierarchical Nanosheet-Assembly Enables Superior Universal Alkali Metal Ion Storage Performance with Multiple Active Sites

Gongrui Wang, Yapeng Li, Shuhong Jiao, Jie Li, Bo Peng Liang Shi* and Genqiang Zhang*

Hefei National Laboratory for Physical Sciences at the Microscale, CAS Key Laboratory of Materials for Energy Conversion,

Department of Materials Science and Engineering, University of Science and Technology of China, Hefei, Anhui 230026, China

*Correspondence: gqzhangmse@ustc.edu.cn;

1. Experimental section

1.1. Materials

Melamine (MA), cyanuric acid (CA), Tin(II) chloride dehydrate ($SnCl_2 \cdot 2H_2O$), and Dimethyl sulfoxide (DMSO) were purchased from Aladdin Industrial Corporation without further purification. Polyvinyl pyrrolidone (PVP, 40000 in Molecular weight) was provided by Sinopharm Chemical Reagent Corporation. Absolute ethanol (99.9%,) was purchased from Aladdin Industrial Corporation without further purification.

1.2. Synthesis of Sn cluster incorporated carbonaceous hierarchical nanosheet-assembly

In a typical synthesis, 4 mmol of MA and 4 mmol of CA were dissolved in 15 mL of DMSO, respectively. Then, a certain amount of PVP and $SnCl_2 \cdot 2H_2O$ (0.5, 0.75, 1.0 mmol) were added into above mentioned MA solution. Subsequently, both of solutions mentioned above were mixed together under continuous stirring at room temperature (25°C), and then the white products were collected after 10 minutes through centrifugation and washed with absolute ethanol. After drying in drying oven overnight, the Sn cluster incorporated carbonaceous hierarchical nanosheet-assembly (denoted as c-SnNC-HNA) can be obtained by pyrolyzing the precursor at various temperature (700, 800, 900 °C) for 2 h with a heating rate of 1 °C min^{-1} in tube furnace in argon atmosphere. The sample without the addition of $SnCl_2 \cdot 2H_2O$ was prepared and other conditions were identical (denoted as NC_{800}).

1.3. Characterizations

The morphology and structure of c-SnNC-HNA and NC_{800} were characterized by field-emission scanning electron microscopy (FESEM, JSM-6700F), transmission electron microscopy (TEM, JOEL JEM-2010; Talos F200X). The structure of c-SnNC-HNA and NC_{800} were characterized by powder X-ray diffraction spectroscopy (XRD, TTR-III) with Cu Kα radiation (V = 40 kV, I = 15 mA) with scan of 10° min^{-1} from 10° to 70° (2θ), Raman spectrometer (LabRamHR, 514 nm excitation laser with a power of 5mW). The surface chemical state of c-SnNC-HNA and NC_{800} were measured by X-ray photoelectron spectroscopy (XPS, ESCALAB 250 X-ray photoelectron spectrometer). The surface area and pore size distribution of c-SnNC-HNA and NC_{800} were calculated through N_2 adsorption-desorption using a Quantachrome instrument (Micrometritics, ASAP 2020) with Brunauer-Emmett-Teller (BET) methods and quenched solid density functional theory (QSDFT) model. Thermos-gravimetric analysis (TG, Mettler-Toledo TGA/DSC 1/1600) was performed in air at a heating rate of 5 °C min^{-1}.

1.4. Electrochemical measurements

The electrochemical performance of the materials was measured in CR2016 coin cells assembled in argon filled glove box with O_2 and H_2O below 0.5 ppm. The working electrode was prepared by spreading the slurry consists of active materials, carbon black (Super-P) and sodium carboxymethylcellulose (CMC) with a mass ratio of 7:2:1 on the copper discs with 12 mm in diameter, followed by drying at 80°C overnight in vacuum drying oven. The active material loading mass of each electrode was controlled to be about 1.5 mg cm^{-2}. For lithium ion batteries (LIBs), metallic lithium foil was used as counter electrode and Celgard 2300 was employed as separator, and the electrolyte was lithium hexafluorophosphate ($LiPF_6$) in ethylene carbonate (EC) and diethyl carbonate (DEC) (with volume ratio of 1:1) with 5 vol% fluoroethylene carbonate (FEC) additive. Metallic sodium foil was applied as counter electrode and 1.0 M $NaClO_4$ in propylene carbonate (PC) with 5 vol% fluoroethylene carbonate (FEC) additive was used as electrolyte for sodium ion batteries (NIBs). Metallic potassium foil was used as counter electrode and 1.0 M potassium bisfluorosulfonylimide (KFSI) in EC and DEC (with volume ratio of 1:1) was used as electrolyte for potassium ion batteries (KIBs). The amount of electrolyte in each cell for LIBs was 50 μL, while those for SIBs/NIBs were 70 μL. The glass fiber (GF/F, Whatman) was used as separator for SIBs and KIBs.

Cyclic voltammetry (CV) measurement was performed on a CHI660E electrochemical workstation. The electrochemical impedance spectroscopy (EIS) was performed in the frequency range between 100 mHz–100 kHz using a CHI660E electrochemical workstation with the a.c. signal kept at an amplitude of 5 mV. Galvanostatic discharge/charge tests (GCD), rate performance and galvanostatic intermittent titration technique (GITT) were conducted on a NEWARE battery test system (CT-4008). For GITT measurement, a series of current pulses at 50 mA g^{-1} for 0.5 h followed by a 1 h relaxation process was applied.

1.5. The potassium ion Hybrid Capacitors

For cathode electrode, activated carbon (AC, 80 wt.%), additive carbon black (10 wt.%) and polyvinylidene fluoride (PVDF, 10 wt.%) binder were mixed to form a uniform slurry and coated on the aluminum discs with a diameter of 16 mm, then, the discs were dried in vacuum oven for 12 hours. The c-SnNC-HNA electrodes were cycled at the current of 200 mA g^{-1} for 5 cycles and discharged to 0.01 V in K-half coin cells. The precycled anode was dissembled in argon-filled glove box, and then KIHCs were

assembled using AC electrode as cathode and precycled c-SnNC-HNA electrodes as anode. 70 μL 1.0 M KFSI in EC and DEC (with volume ratio of 1:1) was used as electrolyte for KIHCs. The glass fiber (GF/F, Whatman) was used as separator. The mass ratio of anode/cathode was fixed to be 1:2, 1:3, 1:4. GCD tests, rate performance and CV tests of the KIHCs device were conducted in the voltage range of 0.1-3.5 V. The specific energy and power density of the KIHCs were calculated by using the equations as follows:

$$E = \int_{t_1}^{t_2} IVdt$$

(S1)

$$P = \frac{E}{t}$$

(S2)

Where E (Wh kg^{-1}) is the energy density and P (W kg^{-1}) is the power density. I is the discharge current density (A g^{-1}), t_1 and t_2 are the start time and terminal time of discharge process, and t (s) is the time period for a full discharge after exclude IR drops.

2. Supplementary figures
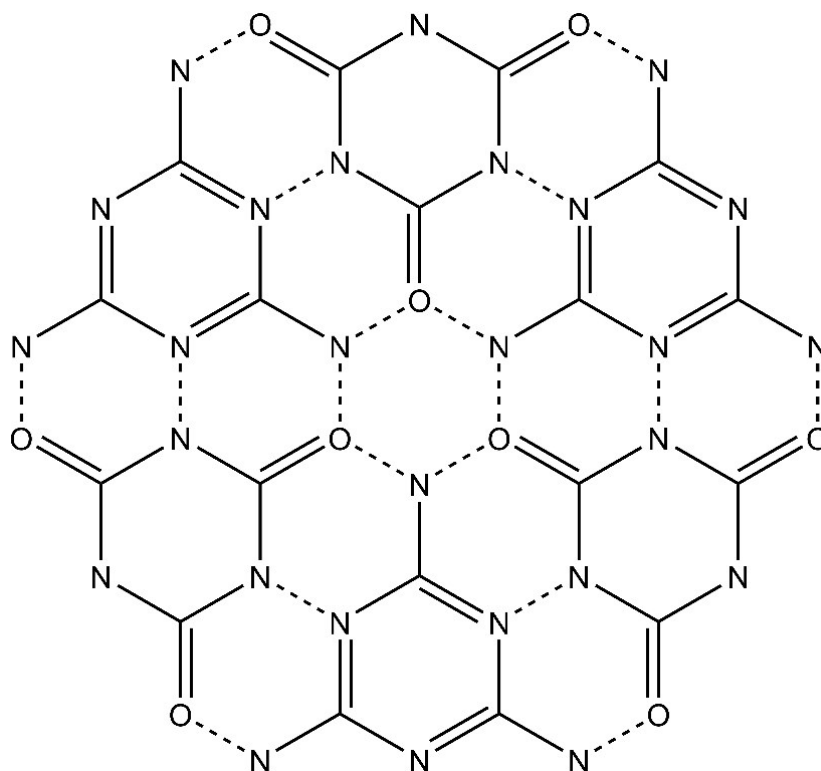
Scheme S1. Chemical formula of melamine-cyanuric acid hydrogen bonded aggregates (MCA). Dotted lines indicate hydrogen bonds.

The formation of these nanosheets could be related to the structure of the molecular assembly of MCA as shown in Scheme S1. Specifically, driven by molecular cooperative assembly between melamine and cyanuric acid with hydrogen bonds of N–H...O and N–H...N linkages, the oblate sphere-like supramolecular assembly can be obtained by mixing melamine and cyanuric acid. The incorporation of Sn is conducted by adding appropriate amount of the $SnCl_2 \cdot 2H_2O$ during the synthesis of MCA through the absorption effect.
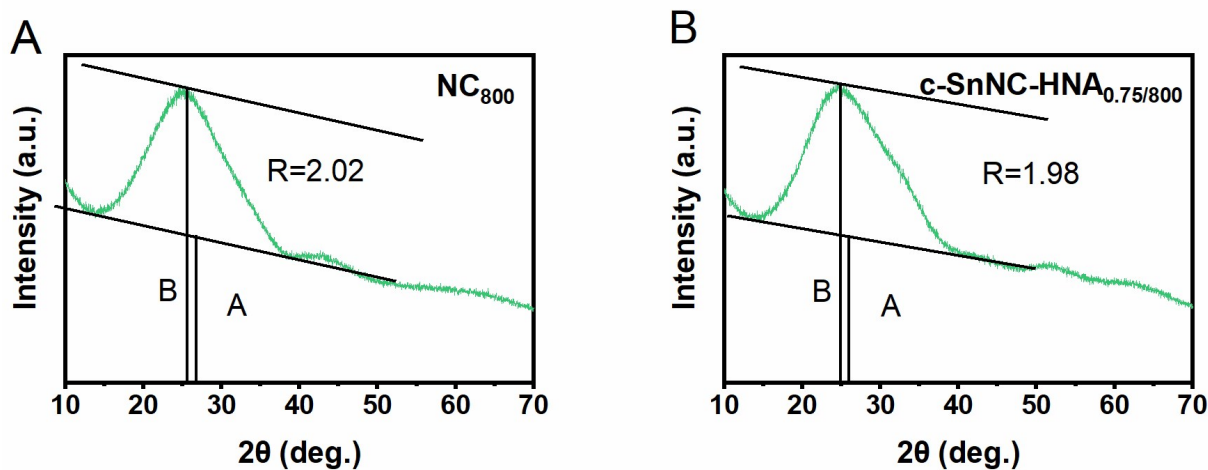
Fig. S1 Illustration of the calculation of the empirical R value.
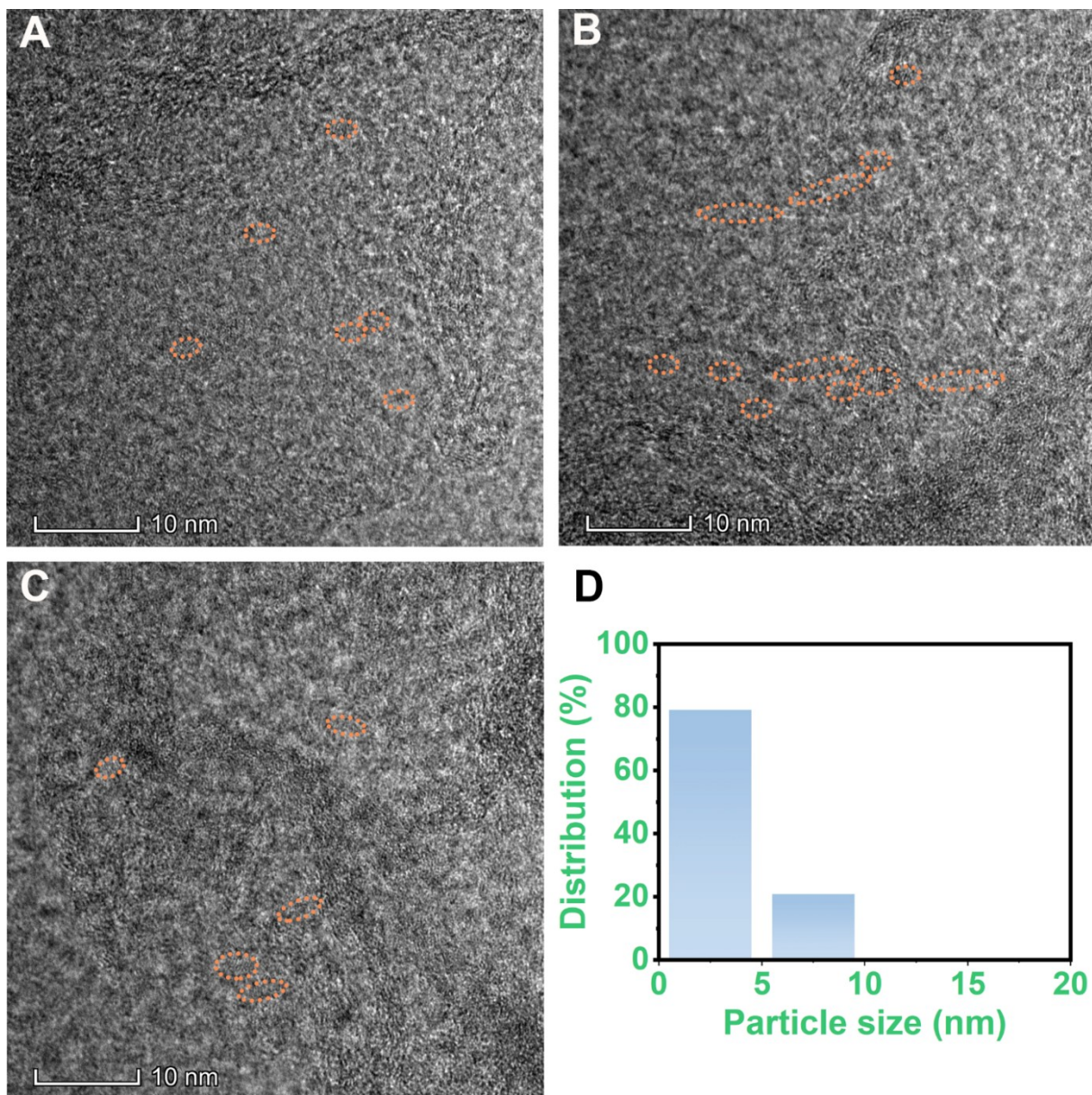
Fig. S2 (A, B, C) HRTEM images of c-SnNC-HNA$_{0.75/800}$ and (D) the size distribution analysis of Sn nanoparticles.
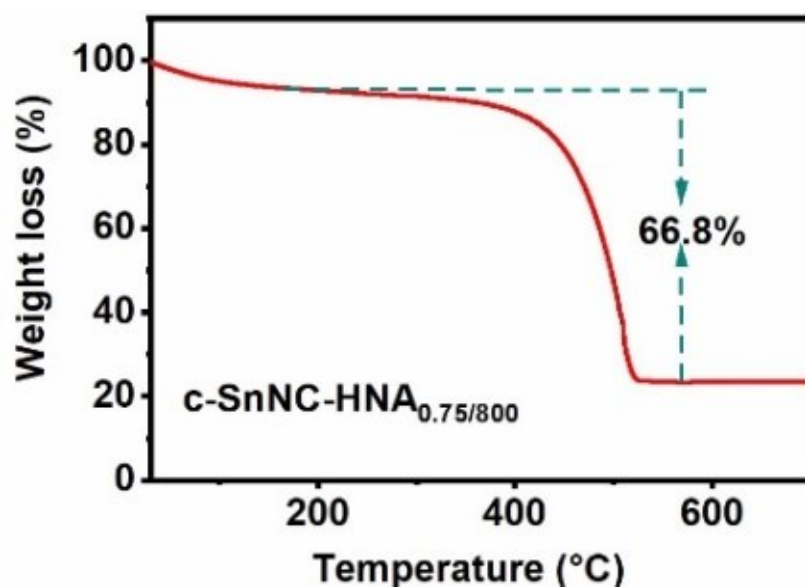
Fig. S3 The thermos-gravimetric analysis of c-SnNC-HNA$_{0.75/800}$.

$$Sn\ (wt\%) = 100\% \times \frac{\text{molecular weight of Sn}}{\text{molecular weight of SnO}_2} \times \frac{\text{final weight of SnO}_2}{\text{initial weight of c - SnNC - HNA}}$$

$$(S3)$$
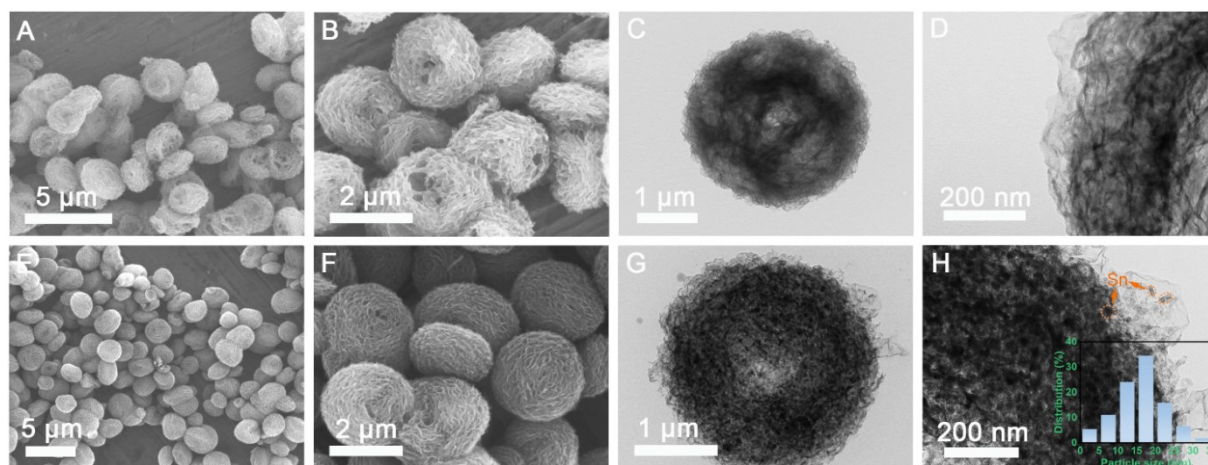
Fig. S4 The morphology and microstructure of c-SnNC-HNA$_{0.75/700}$ and c-SnNC-HNA$_{0.75/900}$: (A, B) FESEM and (C, D) TEM images of c-SnNC-HNA$_{0.75/700}$; (E, F) FESEM and (G, H) TEM images of c-SnNC-HNA$_{0.75/900}$.
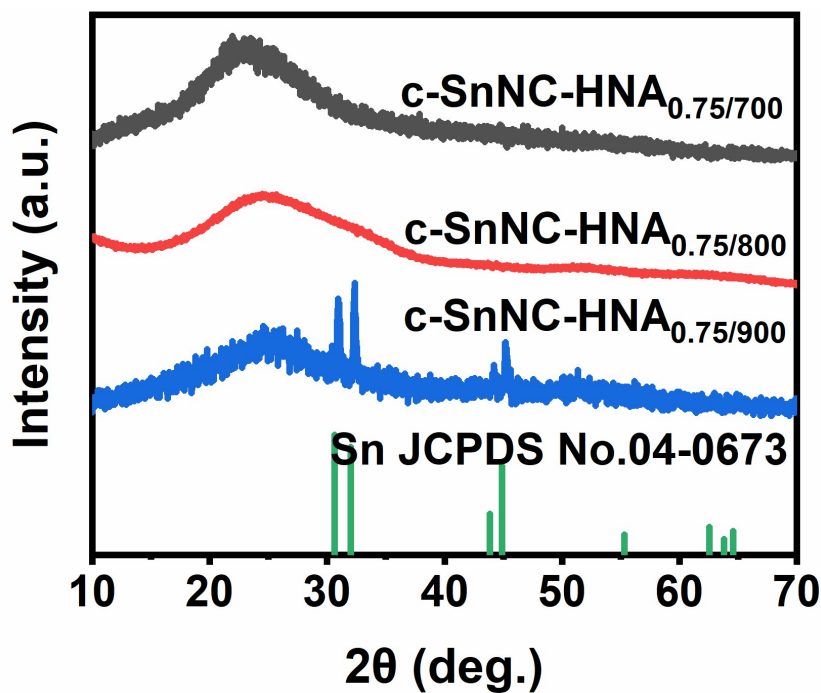
Fig. S5 XRD pattern of the of c-SnNC-HNA at different annealing temperature.

The disappearance of the peaks corresponding to Sn particles of c-SnNC-HNA$_{0.75/700}$ and c-SnNC-HNA$_{0.75/800}$, in contrast to the distinctive peaks of Sn in the patterns of c-SnNC-HNA$_{0.75/900}$ is probably because the Sn species in c-SnNC-HNA$_{0.75/700}$ and c-SnNC-HNA$_{0.75/800}$ are presented in the amorphous state or in a highly dispersed state.[1-3] However, the crystallinity of Sn species becomes well developed upon the annealing temperature rising up, which leads to a distinctive peaks of Sn in the XRD patterns.
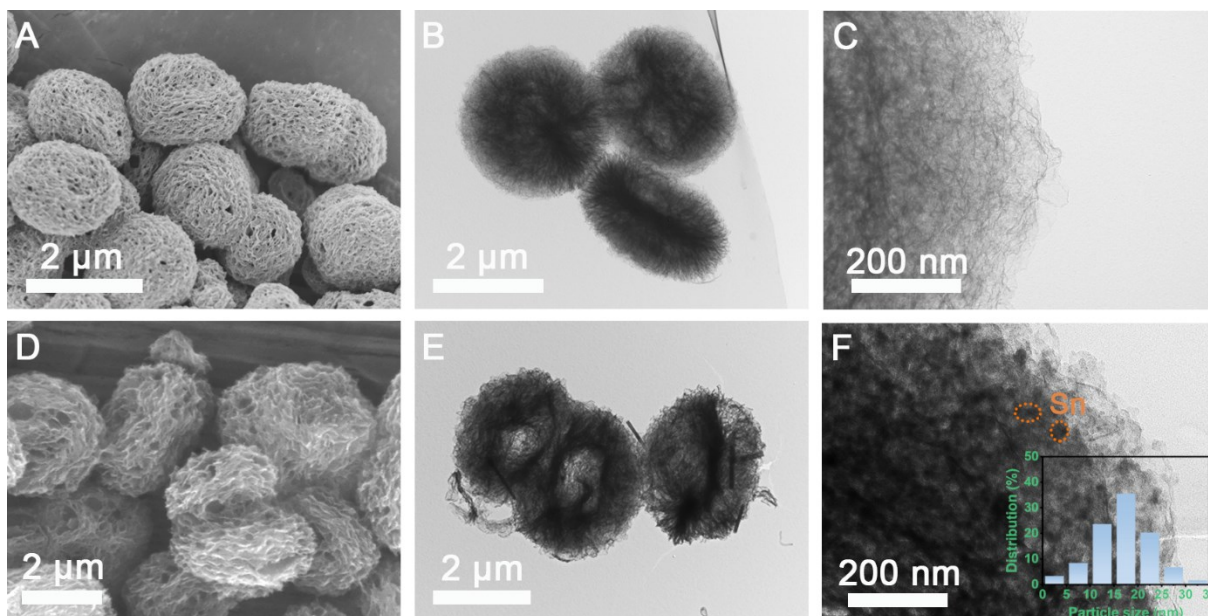
Fig. S6 The morphology and microstructure of c-SnNC-HNA$_{0.5/800}$ and c-SnNC-HNA$_{1/800}$: (A) FESEM and (B, C) TEM images of c-SnNC-HNA$_{0.5/800}$; (D) FESEM and (E, F) TEM images of c-SnNC-HNA$_{1/800}$.

It can be clearly seen that the Sn particles grow up in size with elevating treatment temperature or increasing the amount of SnCl$_2$ 2H$_2$O despite the size distribution of Sn particles in c-SnNC-HNA$_{0.5/800}$ and c-SnNC-HNA$_{0.75/700}$ are estimated according to the TEM images with higher magnifications.
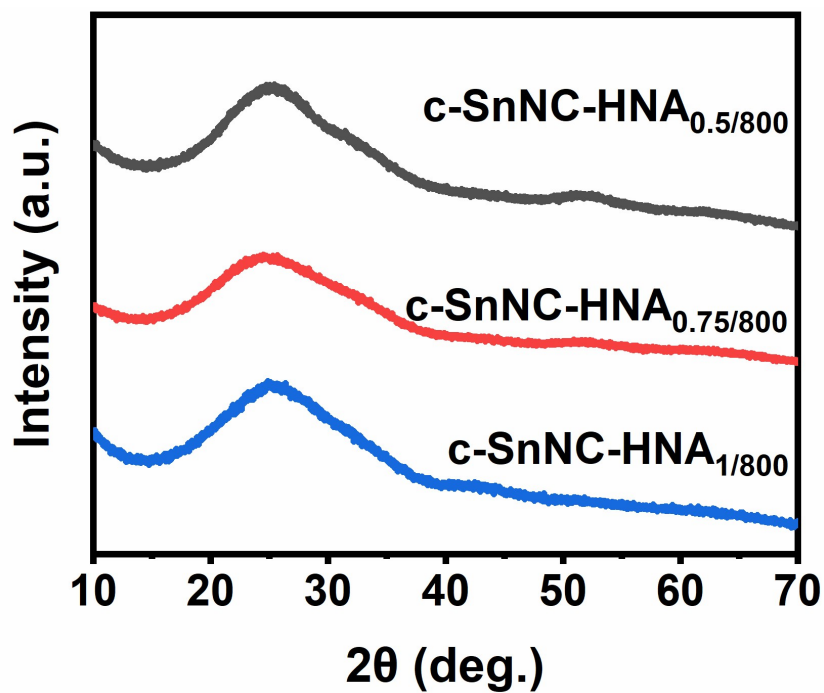
Fig. S7 XRD patterns of (A) c-SnNC-HNA$_{0.5/800}$ and (B) c-SnNC-HNA$_{1/800}$.
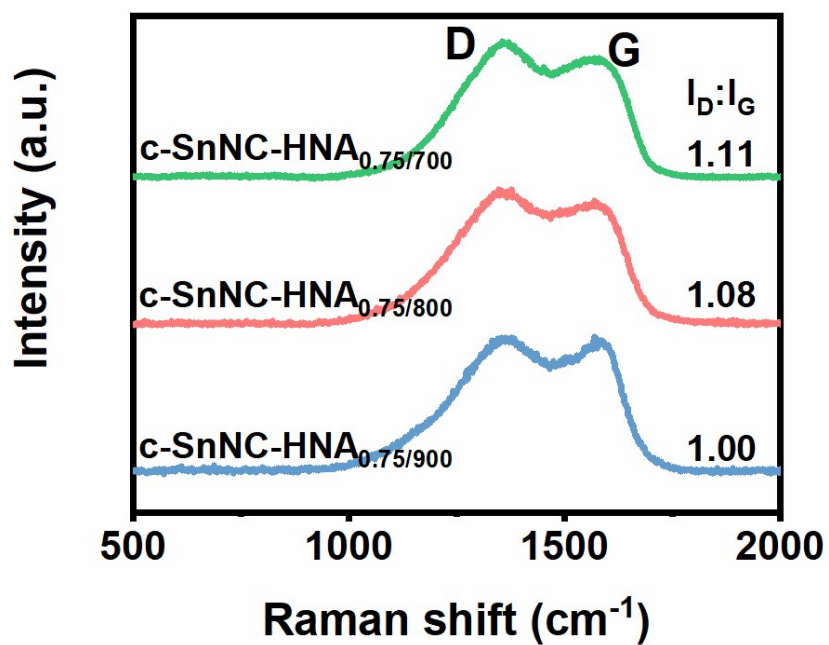
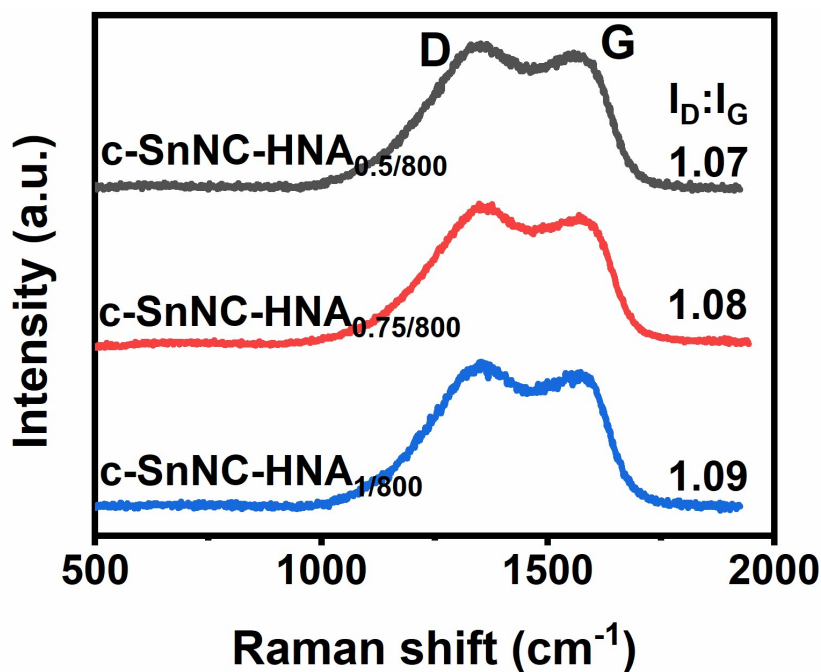**Fig S8** Raman spectra of c-SnNC-HNA at various treating temperatures.

Fig. S9 Raman spectra of c-SnNC-HNA with different amount of $SnCl_2 \cdot 2H_2O$.

The $I_D{:}I_G$ ratio of these samples goes up with the increasing of $SnCl_2 \cdot 2H_2O$, further confirming the incorporation of Sn cluster could lower graphitization degree.
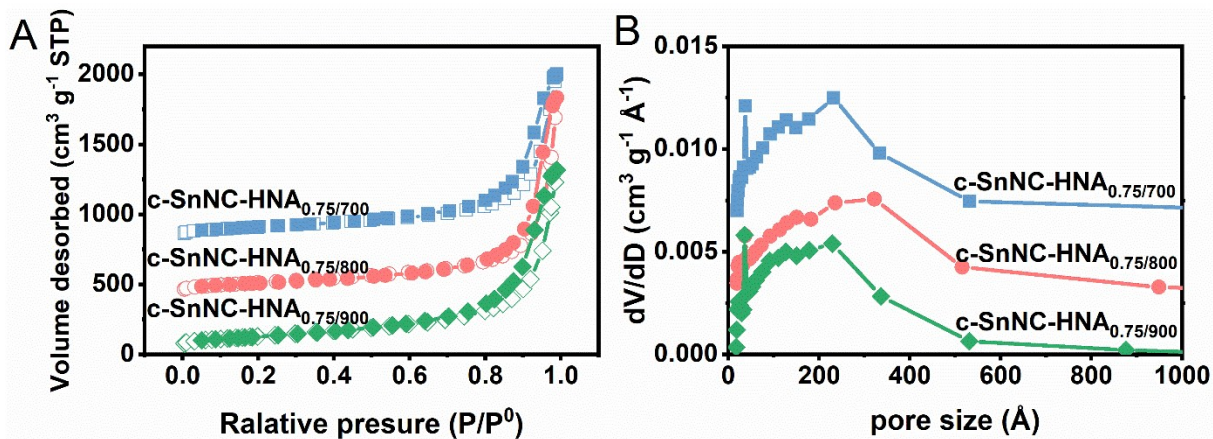

Fig. S10. Nitrogen adsorption-desorption isotherms and the corresponding pore size distribution of c-SnNC-HNA at different annealing temperature.
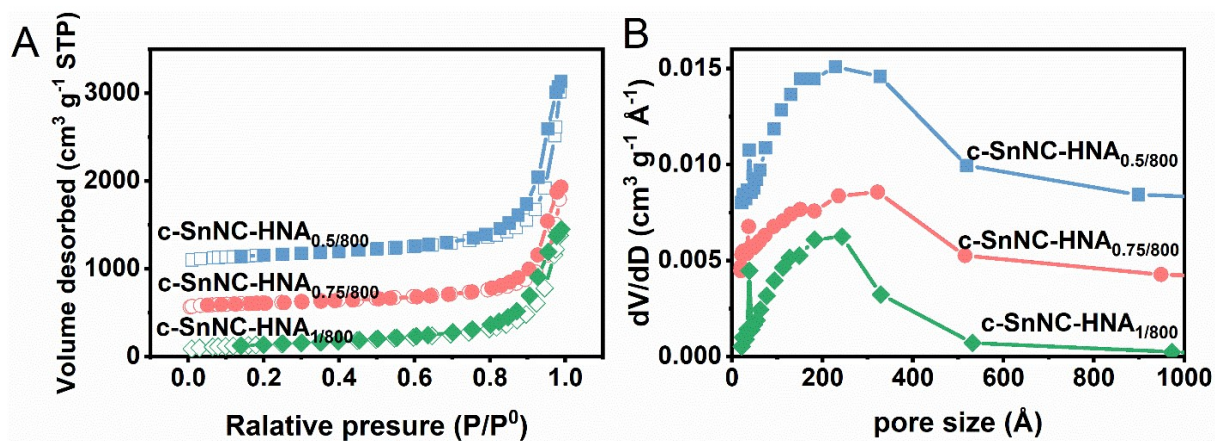
Fig. S11 Nitrogen adsorption-desorption isotherms and the corresponding pore size distribution of c-SnNC-HNA with different content of $SnCl_2 \cdot 2H_2O$.

The porous structure of c-SnNC-HNA is naturally created during the annealing process by the thermal decomposition of –COOH/-NH_2/triazine groups in Sn-MCA and the elimination of the emerged small molecules (i.e. CO_2, NH_3 and etc.) according to the former study based on the melamine and cyanuric acid.[4]
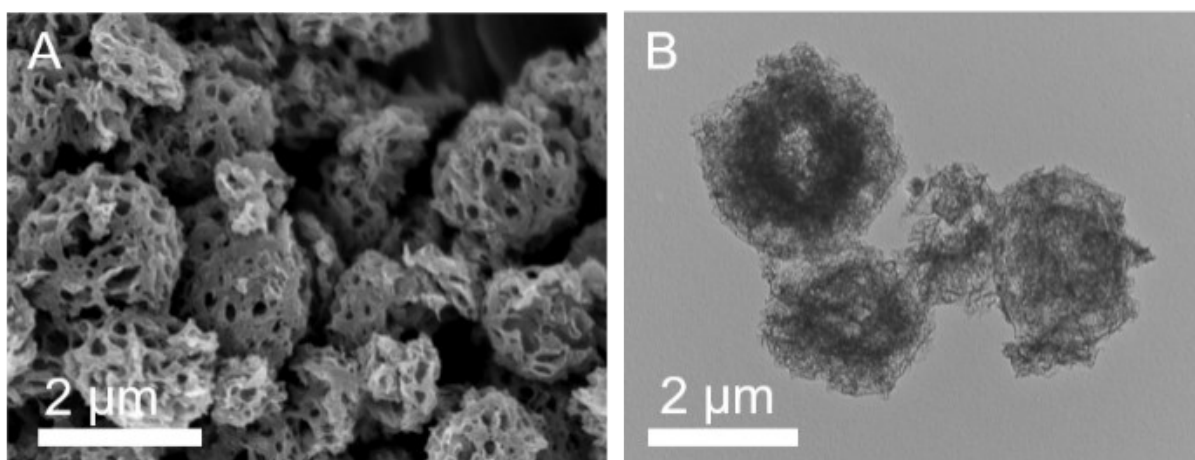
Fig. S12 The morphology and microstructure of NC_{800}: (A) FESEM and (B) TEM images.
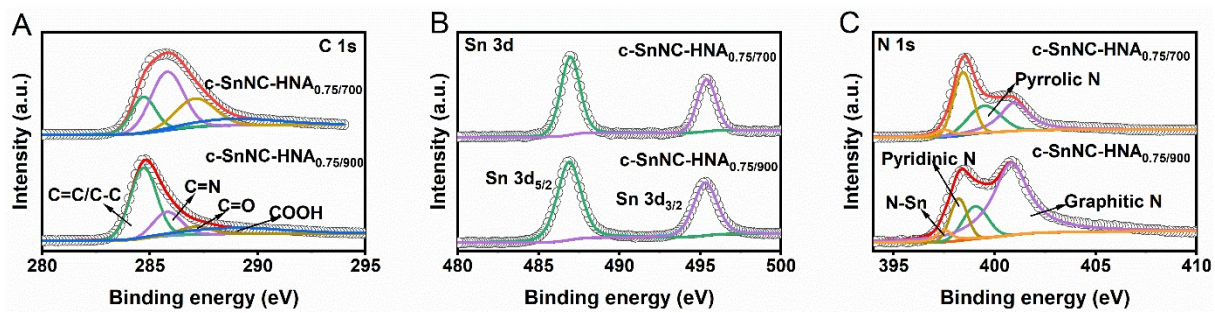
Fig. S13 The high-resolution XPS spectra of c-SnNC-HNA at different annealing temperature: (A) C 1s, (B) Sn 3d and (C) N 1s.
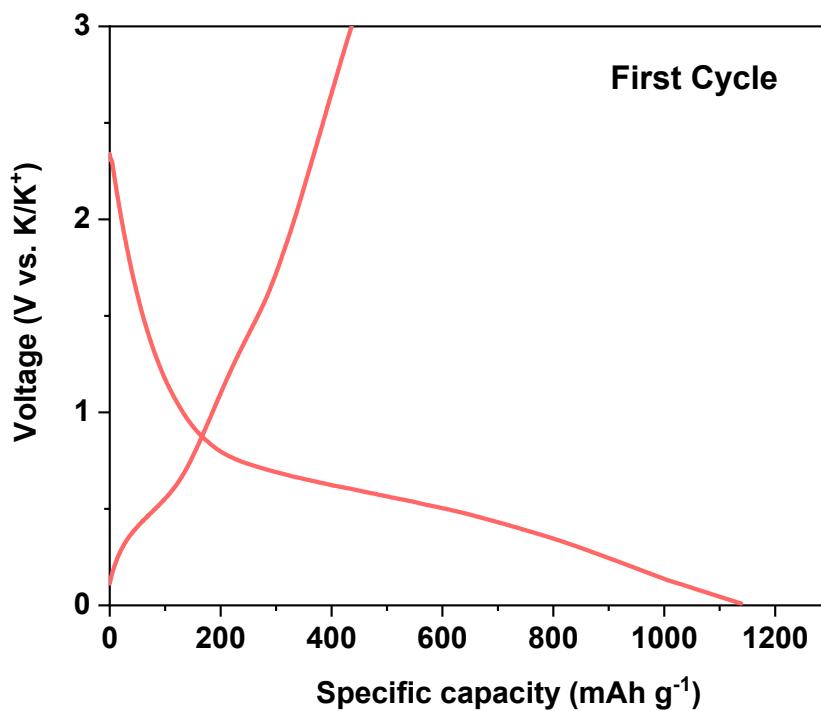
Fig. S14 The initial charge/discharge profiles at 100 mA g^{-1} of c-SnNC-HNA$_{0.75/800}$ for K$^+$ storage.
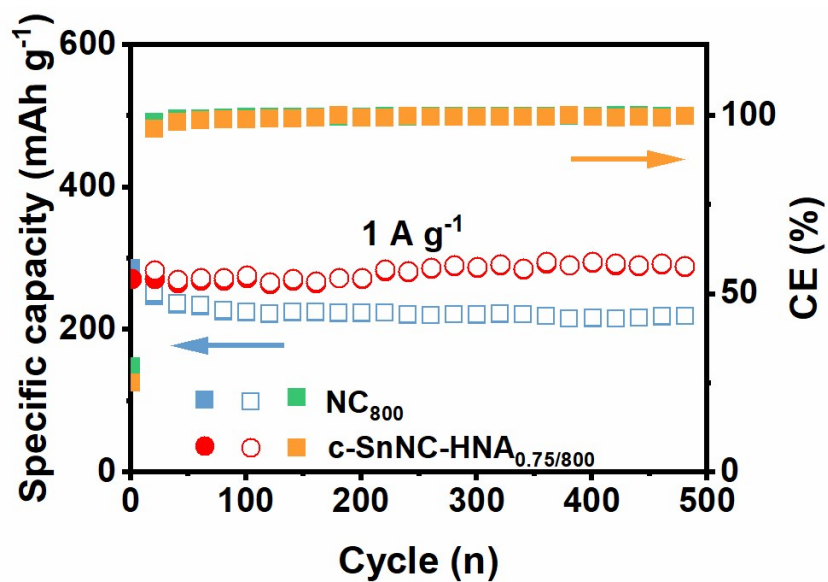

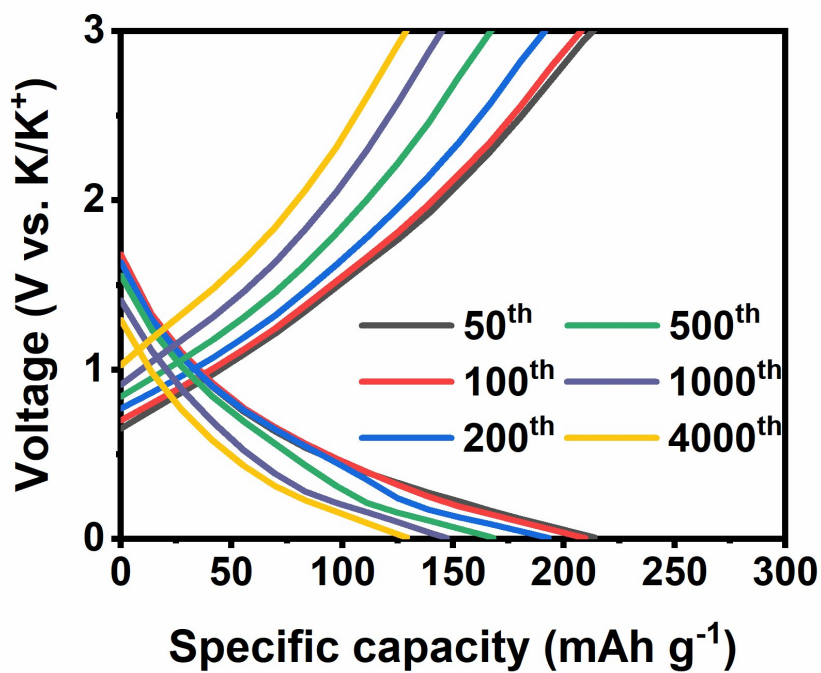**Fig. S15** Cycling stability at 1A g^{-1} for K$^+$ storage.

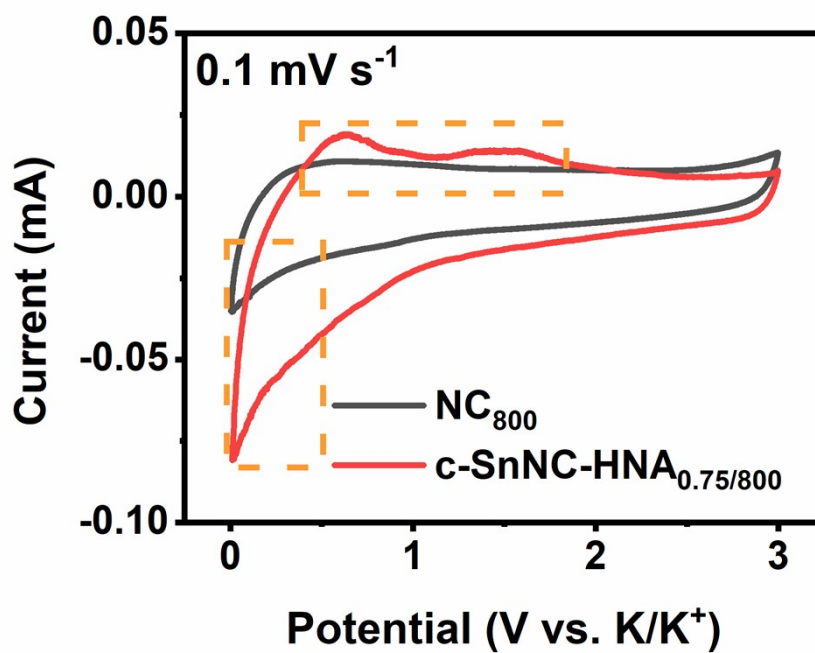**Fig. S16** The charge/discharge profiles at 5 A g^{-1} of c-SnNC-HNA$_{0.75/800}$ for K$^+$ storage.

Fig. S17 The CV comparison of NC$_{800}$ and c-SnNC-HNA$_{0.75/800}$ for K$^+$ storage
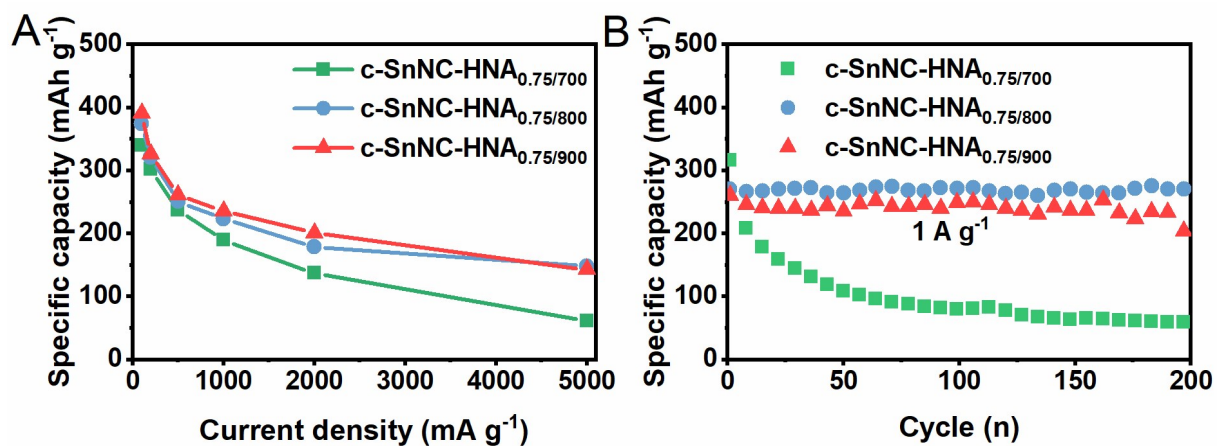
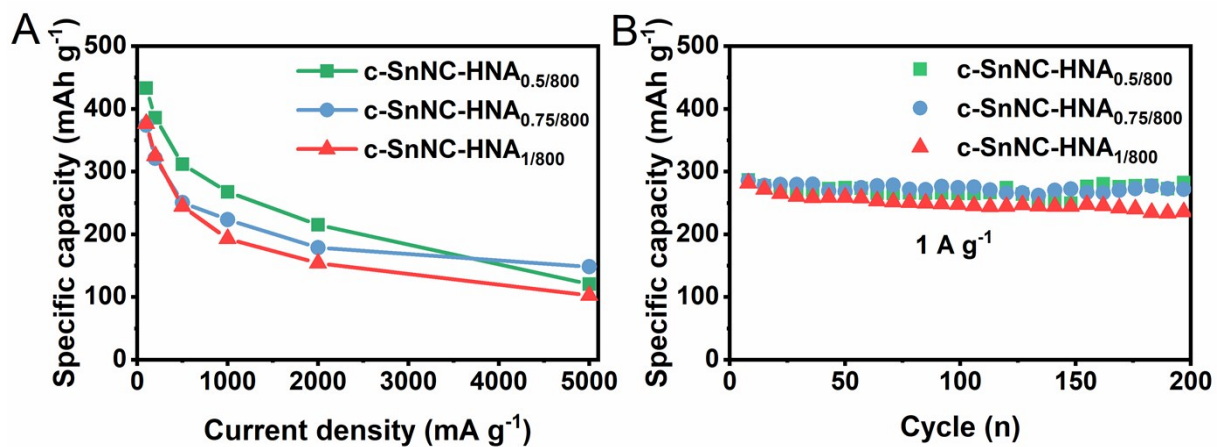**Fig. S18.** Potassium ion storage performance: (A) Rate performance, (B) Cycling stability.

Fig. S19 Potassium ion storage performance: (A) Rate performance, (B) Cycling stability.
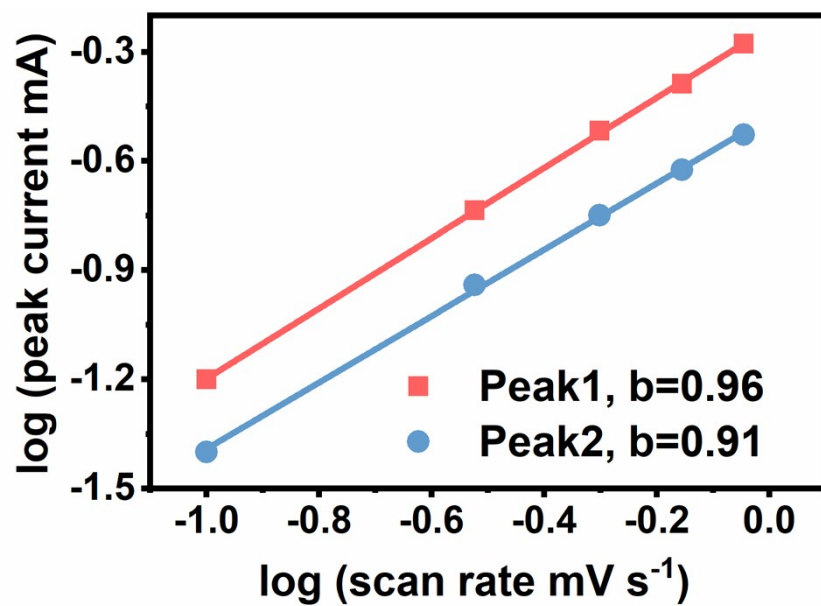
Fig. S20 b-value calculation of c-SnNC-HNA$_{0.75/800}$ for K$^+$ storage.
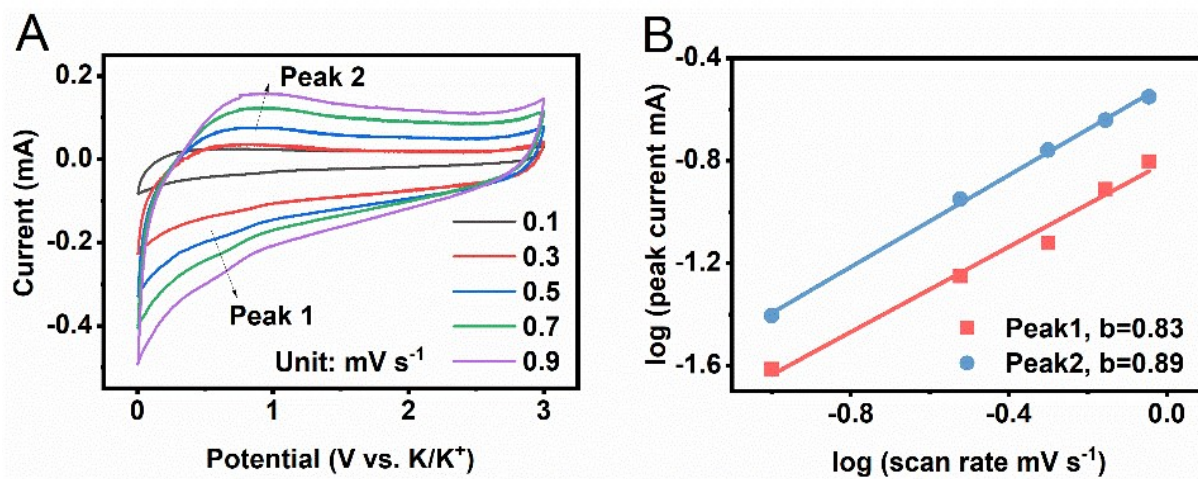

Fig. S21 Potassium ion storage kinetics of NC$_{800}$: (A) CV curves and (B) b-value calculation.
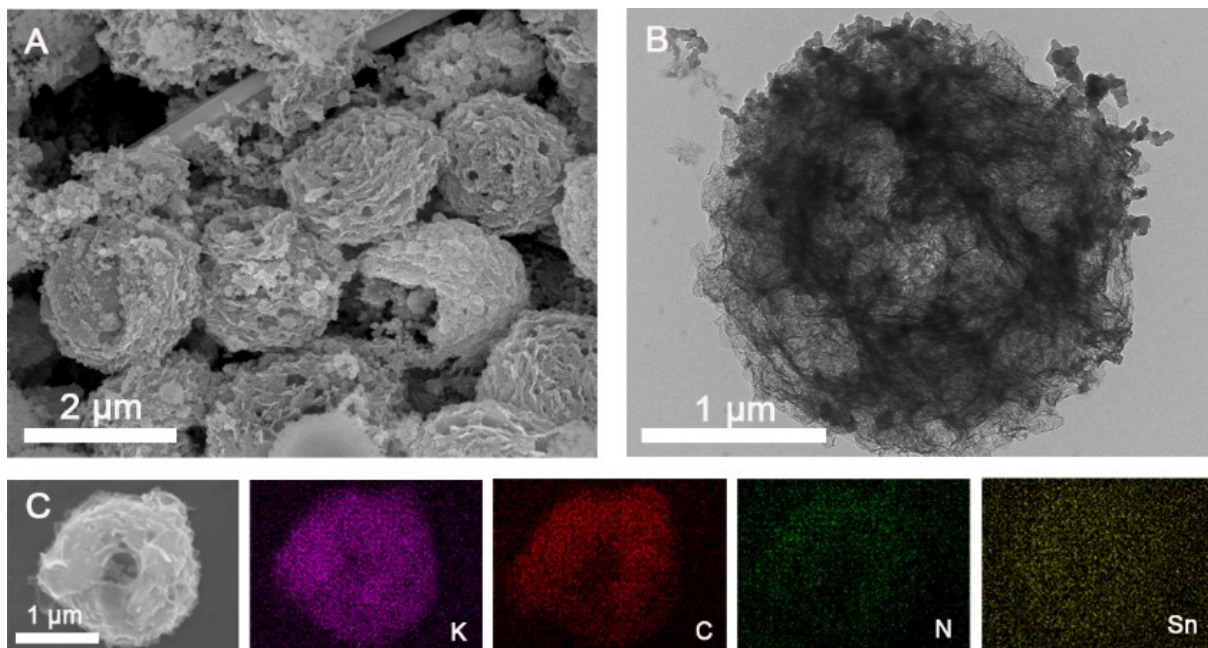
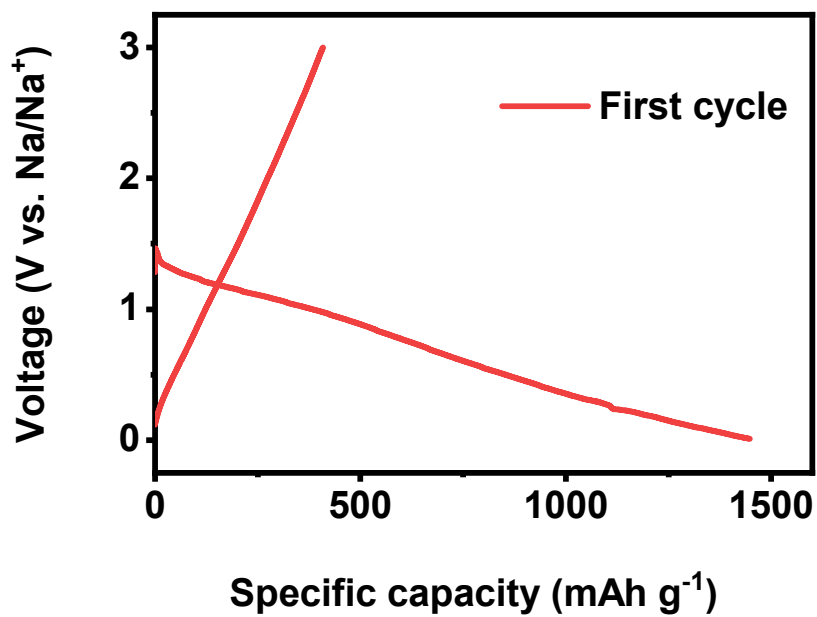**Fig. S22** The SEM image and corresponding elemental mapping results of c-SnNC-HNA$_{0.75/800}$ after 200 cycles at 0.1 A g^{-1} for K$^+$ storage.

Fig. S23 The initial charge/discharge profiles at 100 mA g^{-1} of c-SnNC-HNA$_{0.75/800}$ for Na$^+$ storage.
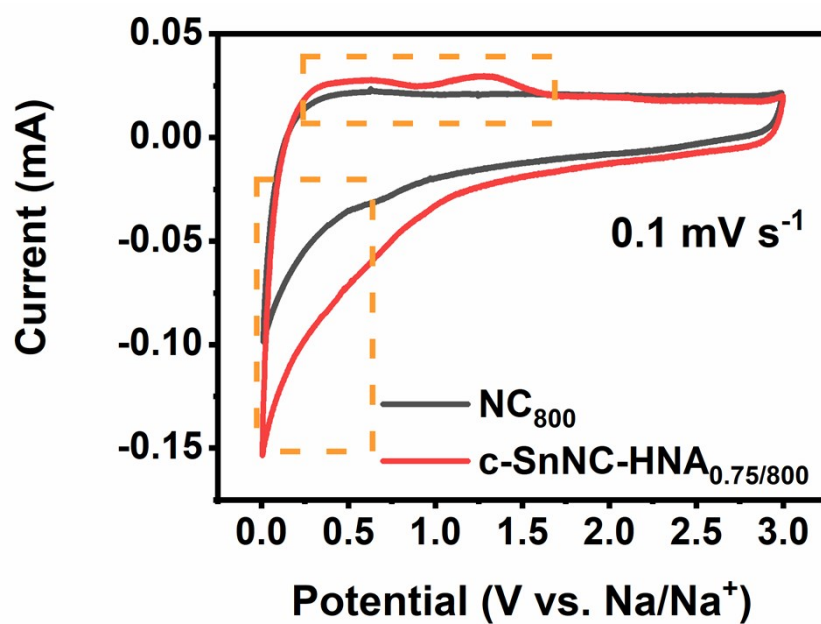
Fig. S24 The CV comparison of NC$_{800}$ and c-SnNC-HNA$_{0.75/800}$ for Na$^+$ storage.
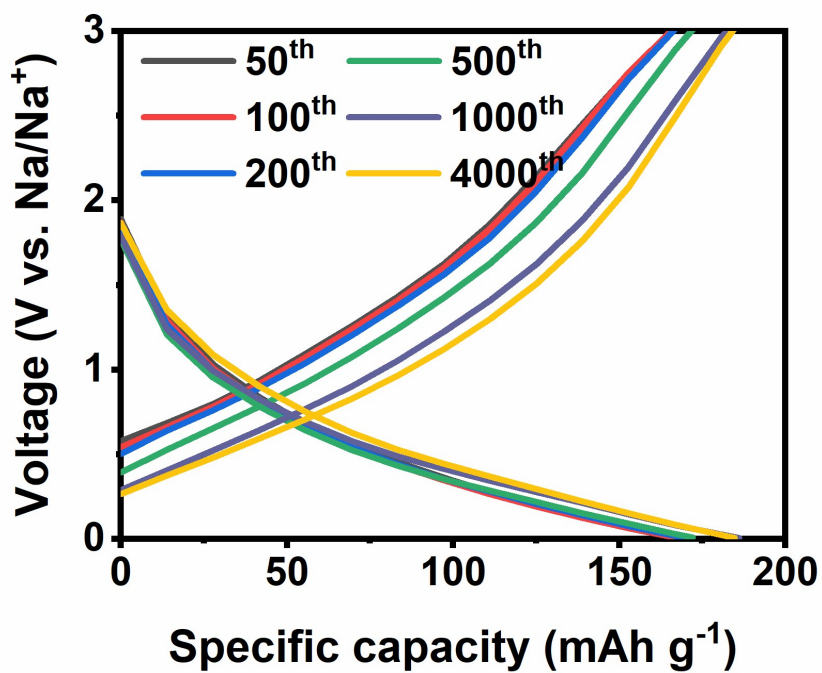
Fig. S25 The charge/discharge profiles at 5 A g^{-1} of c-SnNC-HNA$_{0.75/800}$ for Na$^+$ storage
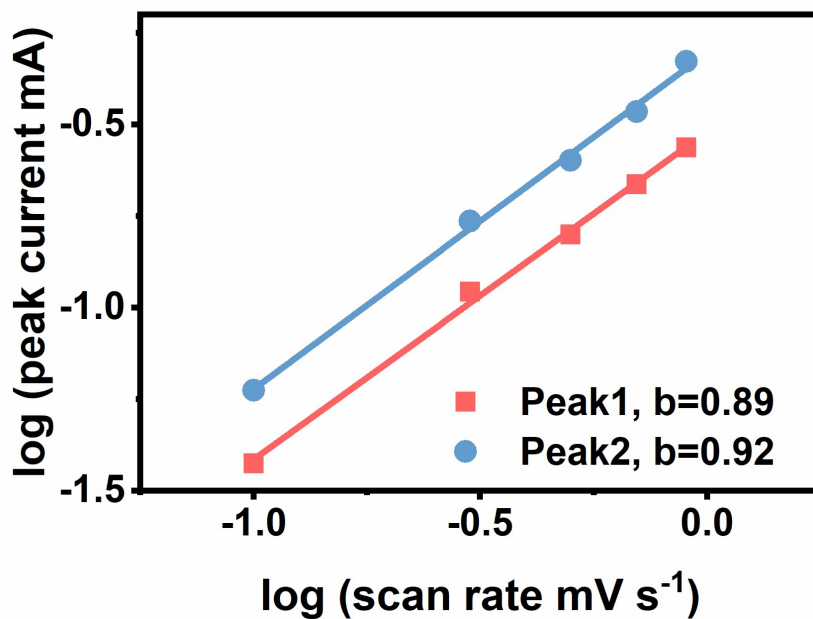

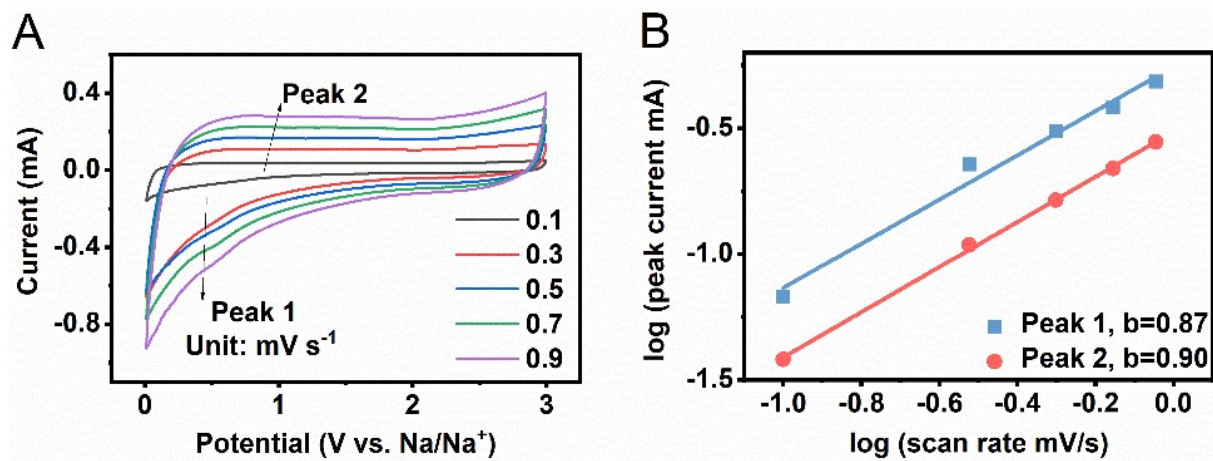**Fig. S26** b-value calculation of c-SnNC-HNA$_{0.75/800}$ for Na$^+$ storage.

Fig. S27 Sodium ion storage kinetics of NC$_{800}$: (A) CV curves, (B) b-value calculation.
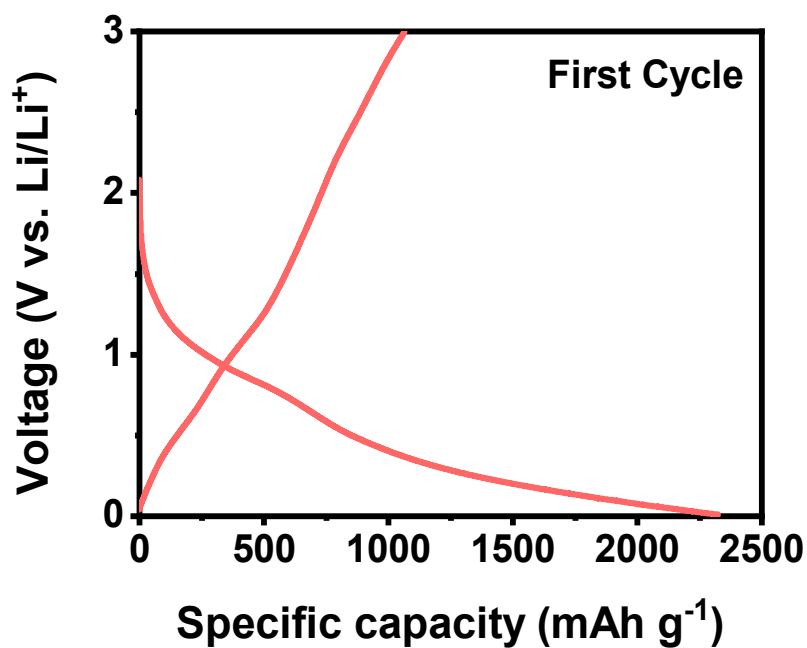
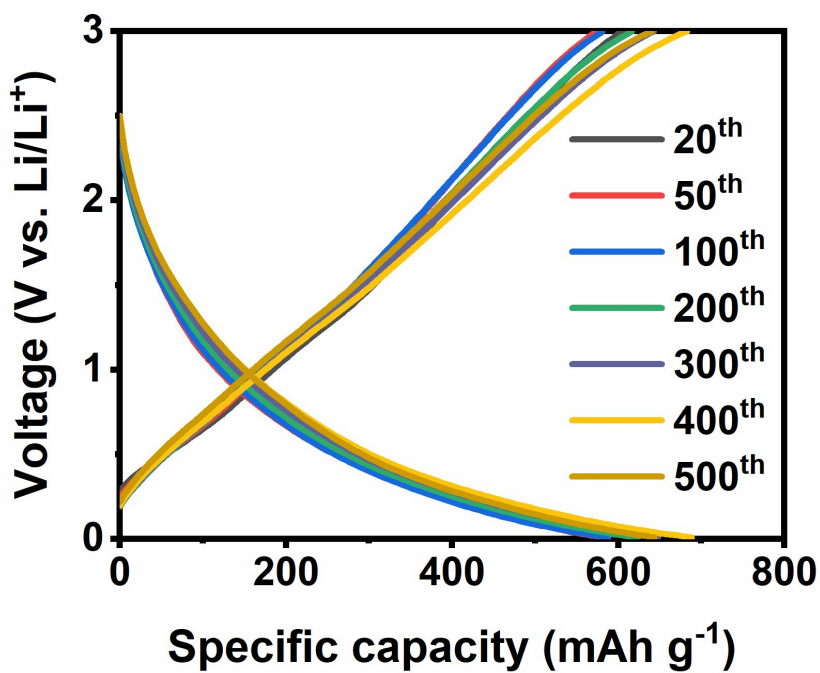**Fig. S28** The initial charge/discharge profiles at 100 mA g^{-1} of c-SnNC-HNA$_{0.75/800}$ for Li$^+$ storage.

Fig. S29 The charge/discharge profiles at 2 A g^{-1} of c-SnNC-HNA$_{0.75/800}$ for Li$^+$ storage
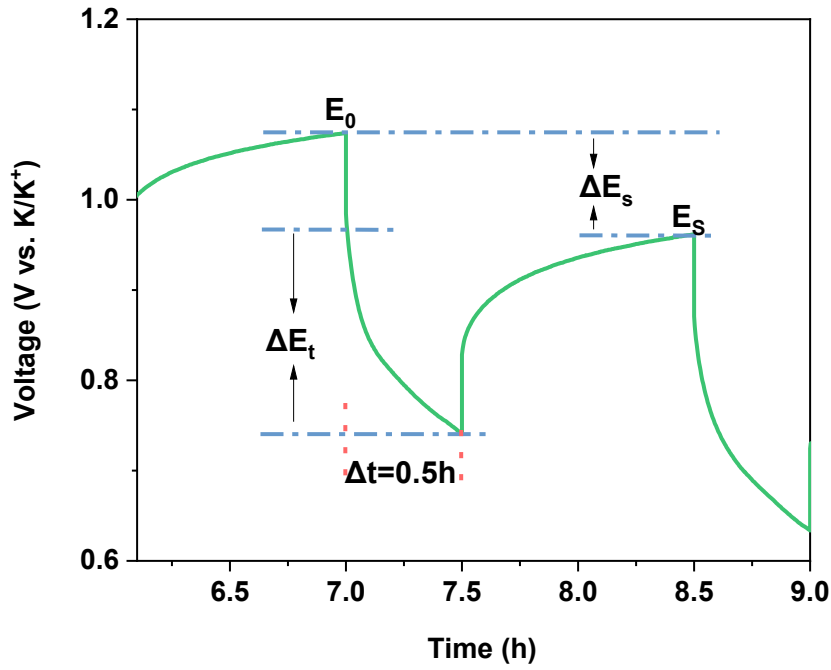
Fig. S30 Current step diagram at 1.35 V of c-SnNC-HNA$_{0.75/800}$ (vs. K/K$^+$) for parameter determination.

The diffusion coefficient (*D*) of c-SnNC-HNA electrode is calculated from the GITT potential profiles using Fick's second law with the following equation:

$$D = \frac{4}{\pi\tau}\left(\frac{m_B V_M}{M_B S}\right)^2\left(\frac{\Delta E_S}{\Delta E_\tau}\right)^2$$

(S4)

τ^0 (s) is the pulse duration, m_B, M_B and V_M are the mass (g), the molar mass (g mol^{-1}) and the molar volume (mL mol^{-1}) of the active materials, and S is the active surface area (cm^2) of the working electrodes. ΔE_S (V) is the potential difference of two adjacent steady states, and $\Delta E\tau$ (V) is the potential change owing to the pulse current. The value of M_B/V_M can be obtained from the density of c-SnNC-HNA. The density of c-SnNC-HNA was calculated based on the following equation:

$$\rho = \frac{1}{V_{total} + \frac{1}{\rho_{carbon}} + \frac{1}{\rho_{Sn}}}$$

(S5)

where ρ (g cm^{-3}) is the density of c-SnNC-HNA, V_{total} (cm^3 g^{-1}) is the total pore volume measured from the N$_2$ isotherm, and ρ_{carbon} is the true density of carbon (2 g cm^{-3}).
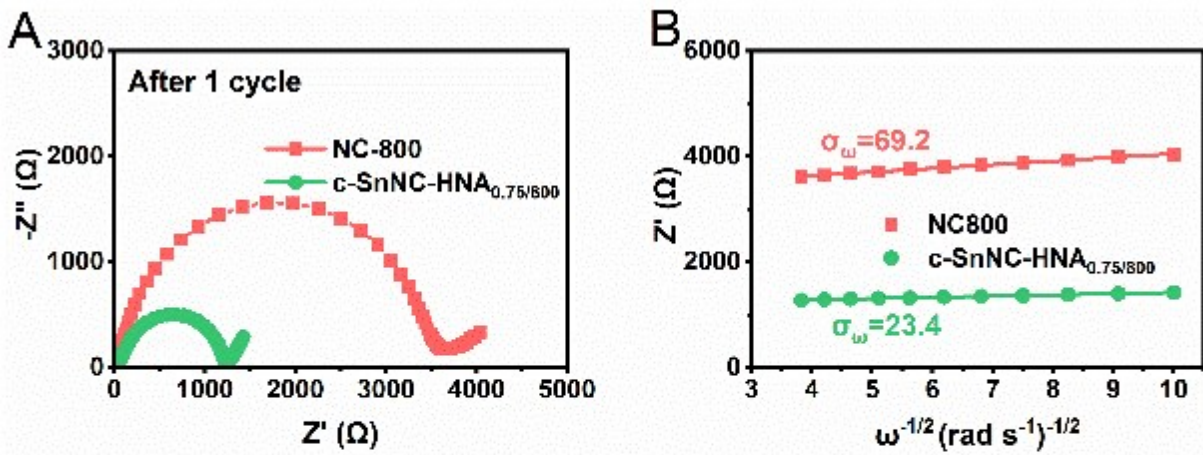
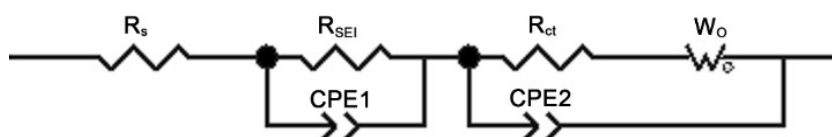**Fig. S31** (A) Nyquist plots and (B) σ_w calculation of c-SnNC-HNA$_{0.75/800}$ and NC$_{800}$.

Fig. S32 The corresponding equivalent circuit.

The Nyquist plots of c-SnNC-HNA$_{0.75/800}$ and NC$_{800}$ were obtained after 1 cycles at 100 mA g^{-1} (**Fig. S31**, Supporting Information), where a classic semicircle at high to medium frequency range was assigned to charge transfer impedance (R$_{ct}$) on the interface between electrode and electrolyte, while a linear Warburg component (W$_O$) at low frequency range corresponded to the diffusion of K$^+$ inside the electrode.[5, 6] The Nyquist plot was fitted using an equivalent circuit (**Fig. S32**, Supporting Information). According to previous studies, the K$^+$ diffusion coefficient can be represented by σ$_ω$ based on the following equations:[7]

$$D_{K^+} = \frac{R^2T^2}{2A^2n^4F^4C^2\sigma_w^2}$$

(S6)

$$Z' = R_e + R_{ct} + \sigma_w\omega^{-\frac{1}{2}}$$

(S7)

Where R, T and F are gas constant, absolute temperature and Faraday constant, respectively. n is the number of electrons transferred per molecule of the active material during the reaction. A and C are the area and K$^+$ concentration of the electrolyte. ω is the angular frequency. σ$_ω$ is the Warburg factor, which can be obtained from the slope of ω$^{-1/2}$ vs. Z in the low frequency range (equation 7). Based on equation (6) and (7), the smaller the σ$_ω$ is, the bigger the D$_K^+$ is. As shown in **Fig. S31** and corresponding **Table S2** in Supporting Information, clearly, c-SnNC-HNA$_{0.75/800}$ electrode has a smaller Rct and σ$_ω$ value than NC$_{800}$ electrode, meaning the superior kinetic properties at the interface of electrode/electrolyte, which benefit from not only the well contact between electrode/electrolyte and improved transportation of electrolyte supplied by hierarchical porous structure, but the fast charge storage reaction furnished by uniformly distributed Sn cluster.
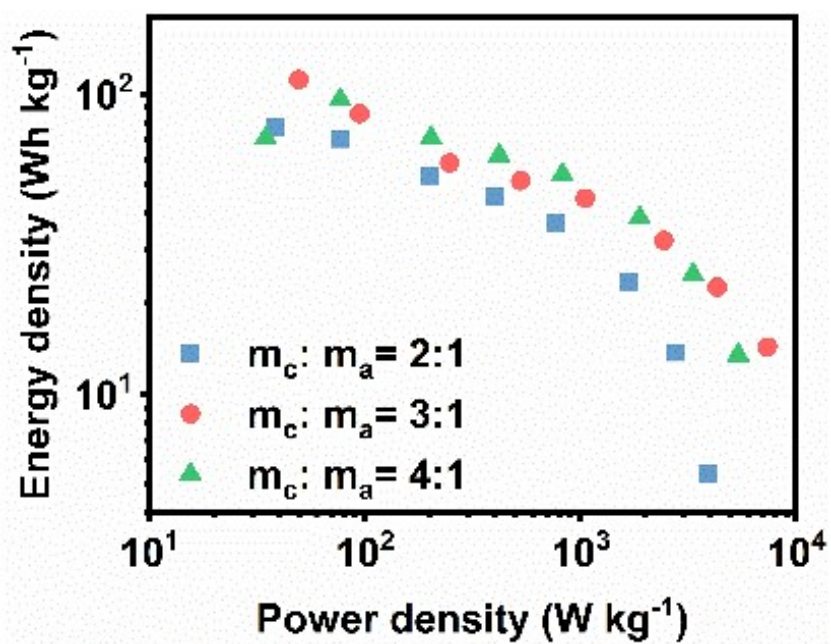
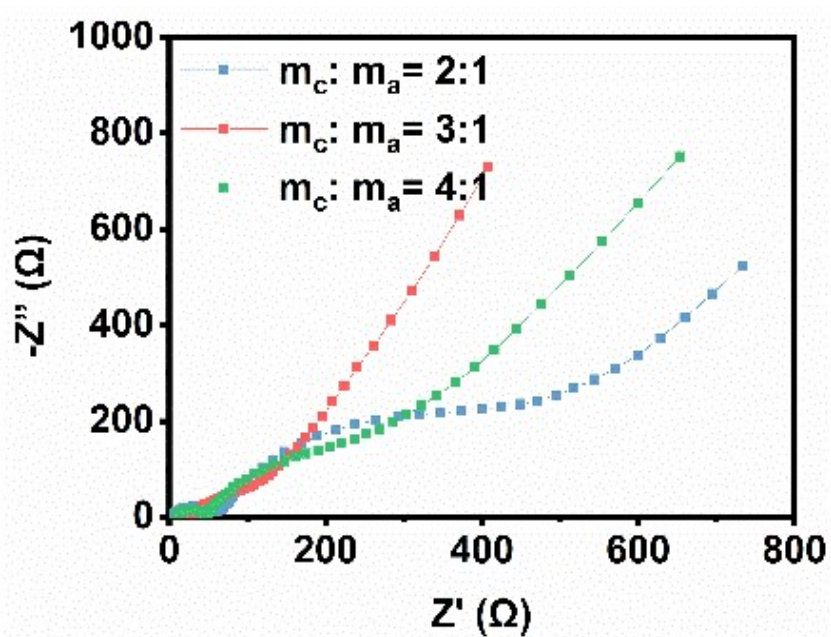**Fig. S33** Ragone plot of KIHCs with various m_c: m_a ratio

Fig. S34 Nyquist plot of KIHCs with various m_c: m_a ratio after 5 cycles at 100 mA g^{-1}.
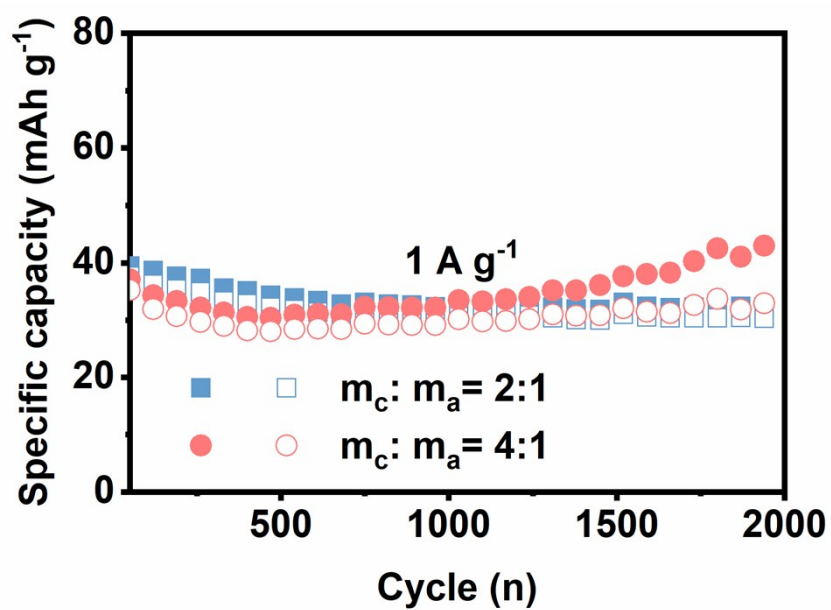
Fig. S35 Cycling performance of KIHCs with (A) m_c: m_a ratio=2:1, (B) m_c: m_a ratio=4:1.

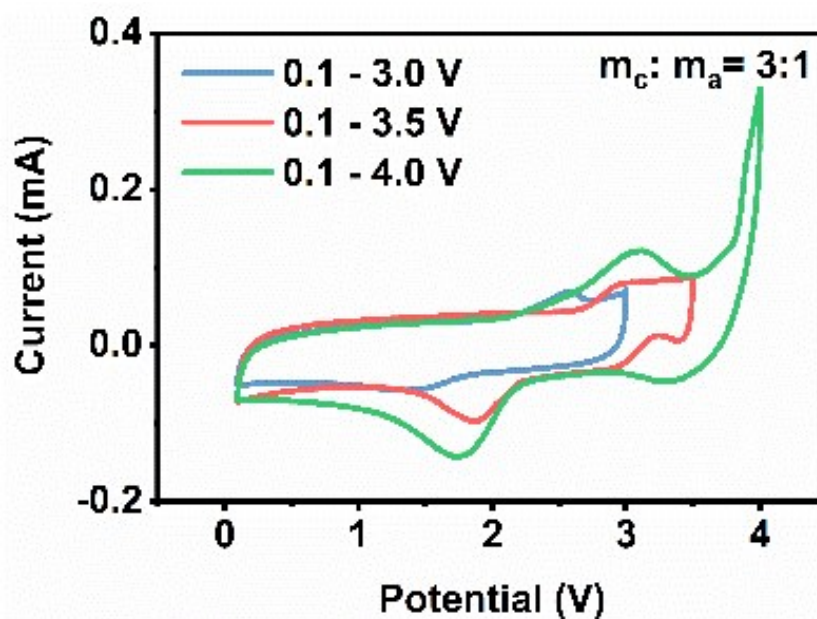**Fig. S36** CV curves at 0.5 mV s^{-1} between various voltage window of KIHCs with m_c: m_a ratio of 3:1.
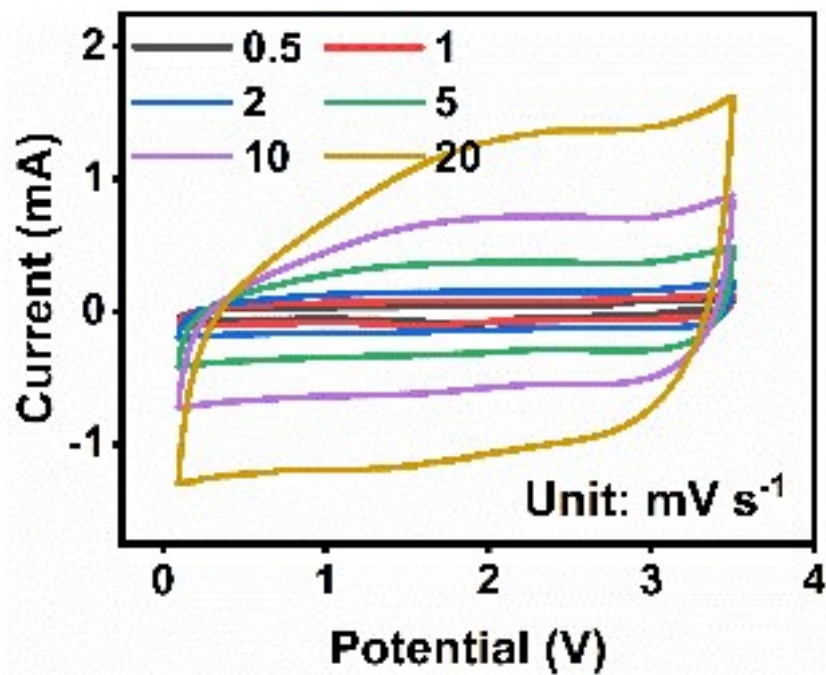
Fig. S37 CV curves at various scan rate between 0.1-3.5 V of KIHCs: (A) m_c: m_a ratio=3:1.
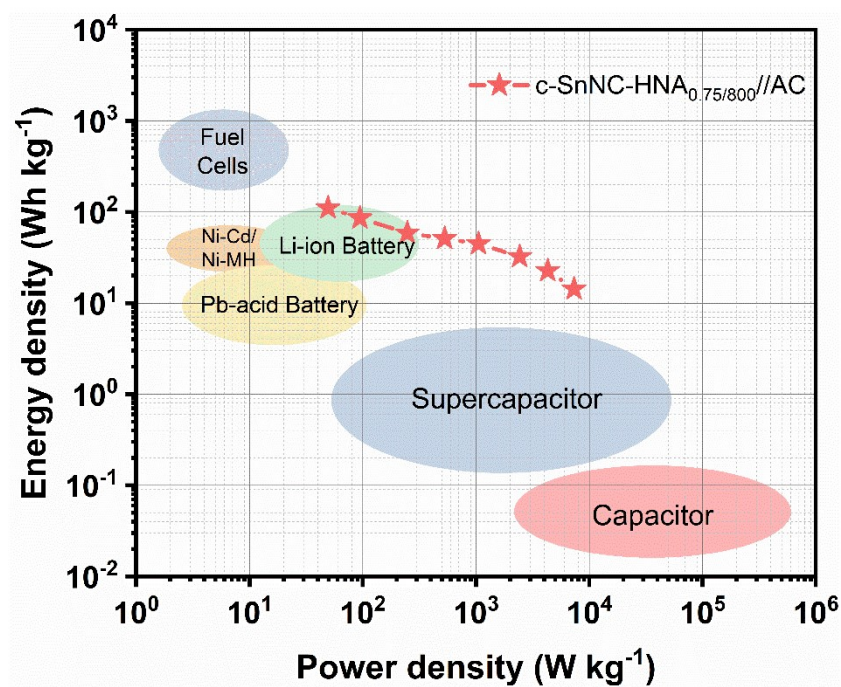

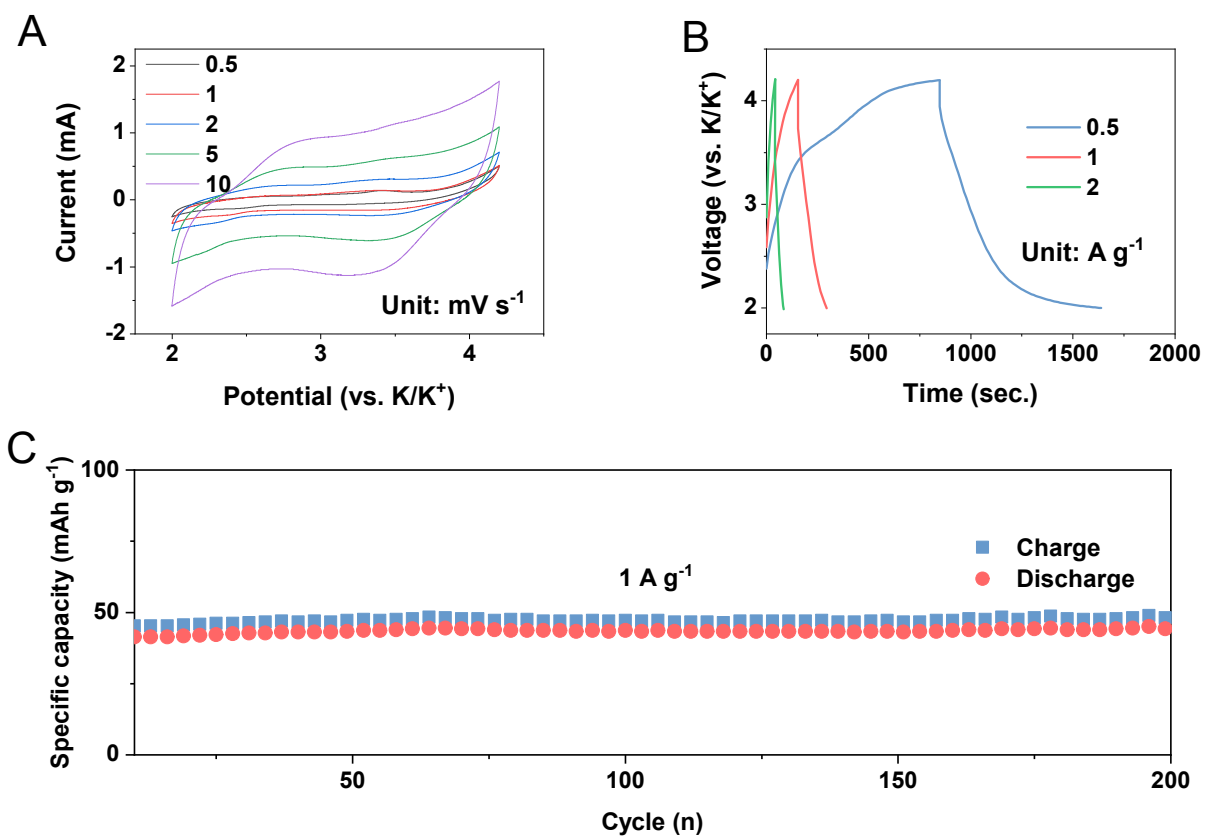**Fig. S38** Comparison of different battery chemistry.

Fig. S39. Potassium ion storage performance of active carbon cathode: (A) CV curves, (B) charge/discharge profiles and (C) cycling performance at 1 A g^{-1}.

Table S1. The comparison of potassium ion storage performance between c-SnNC-HNA$_{0.5/800}$ and other carbonaceous based electrode materials.

Material	Capacity (mAh g^{-1})/ current (A g^{-1})	Capacity (mAh g^{-1}) /rate (A g^{-1})	Capacity (mAh g^{-1}) /Cycles/current (A g^{-1})	References
c-SnNC-HNA$_{0.75/800}$	436.2/0.1	151.4/5	129.2/4000/5	This paper
PNHC	419.3/0.1	119.5/10	270.4/1000/1	[8]
HCNT	232/0.1	162/1.6	210/500/0.1	[9]
S/N@C	350/0.05	64/4	65/900/2	[10]
NHC	293.5/0.1	204.8/2	161.3/1600/1	[11]
Fe$_3$C@PGC-NGF	300/0.5	195/1	155/10000/1	[12]
NCS	205/0.033	154/20.16	180/4000/0.504	[13]
NOHPHC	365/0.25	118/3	125/1100/1.050	[14]
NCNF-650	368/0.25	101/20	146/4000/2A	[15]

Table S2. Fitting results of c-SnNC-HNA and NC$_{800}$ after ten cycles.

Samples	R$_s$(Ω)	R$_{SEI}$(Ω)	R$_{ct}$(Ω)
NC$_{800}$	32.0	64.39	3455
c-SnNC-HNA$_{0.75/800}$	8.38	63.3	1153

References:

1. Y. Xue, Y. Li, G. Luo, K. Shi, E. Liu and J. Zhou, *Adv. Energy Mater.*, 2020, 2002644.

2. D. A. Bulushev, A. L. Chuvilin, V. I. Sobolev, S. G. Stolyarova, Y. V. Shubin, I. P. Asanov, A. V. Ishchenko, G. Magnani, M. Riccò,

   A. V. Okotrub and L. G. Bulusheva, *J. Mater. Chem. A*, 2017, **5**, 10574-10583.

3. T. Wang, R. Yang, N. Shi, J. Yang, H. Yan, J. Wang, Z. Ding, W. Huang, Q. Luo, Y. Lin, J. Gao and M. Han, *Small*, 2019, **15**, e1902410.

4. S. Guo, Z. Deng, M. Li, B. Jiang, C. Tian, Q. Pan and H. Fu, *Angew. Chem. Int. Ed. Engl.*, 2016, **55**, 1830-1834.

5. Y. Chu, L. Guo, B. Xi, Z. Feng, F. Wu, Y. Lin, J. Liu, D. Sun, J. Feng, Y. Qian and S. Xiong, *Adv. Mater.*, 2018, **30**, 1704244.

6. K. Kaup, F. Lalère, A. Huq, A. Shyamsunder, T. Adermann, P. Hartmann and L. F. Nazar, *Chem. Mater.*, 2018, **30**, 592-596.

7. X. Zhao, W. Cai, Y. Yang, X. Song, Z. Neale, H.-E. Wang, J. Sui and G. Cao, *Nano Energy*, 2018, **47**, 224-234.

8. H. He, D. Huang, Y. Tang, Q. Wang, X. Ji, H. Wang and Z. Guo, *Nano Energy*, 2019, **57**, 728-736.

9. M. G. Boebinger, D. Yeh, M. Xu, B. C. Miles, B. Wang, M. Papakyriakou, J. A. Lewis, N. P. Kondekar, F. J. Q. Cortes, S. Hwang, X.

   Sang, D. Su, R. R. Unocic, S. Xia, T. Zhu and M. T. McDowell, *Joule*, 2018, **2**, 1-17.

10. A. Mahmood, S. Li, Z. Ali, H. Tabassum, B. Zhu, Z. Liang, W. Meng, W. Aftab, W. Guo, H. Zhang, M. Yousaf, S. Gao, R. Zou and

   Y. Zhao, *Adv. Mater.*, 2019, **31**, 1805430.

11. W. Yang, J. Zhou, S. Wang, W. Zhang, Z. Wang, F. Lv, K. Wang, Q. Sun and S. Guo, *Energy Environ. Sci.*, 2019, **12**, 1605-1612.

12. K. Han, Z. Liu, P. Li, Q. Yu, W. Wang, C.-Y. Lao, D. He, W. Zhao, G. Suo, H. Guo, L. Song, M. Qin and X. Qu, *Energy Stor. Mater.*,

   2019, **22**, 185-193.

13. S. Chen, C. Wu, L. Shen, C. Zhu, Y. Huang, K. Xi, J. Maier and Y. Yu, *Adv. Mater.*, 2017, **29**, 1700431.

14. J. Yang, Z. Ju, Y. Jiang, Z. Xing, B. Xi, J. Feng and S. Xiong, *Adv. Mater.*, 2018, **30**, 1700104.

15. Y. Xu, C. Zhang, M. Zhou, Q. Fu, C. Zhao, M. Wu and Y. Lei, *Nat. Commun.*, 2018, **9**, 1720.